Microporous and Mesoporous Materials 341 (2022) 112043

Contents lists available at ScienceDirect

Microporous and Mesoporous Materials

journal homepage: www.elsevier.com/locate/micromeso

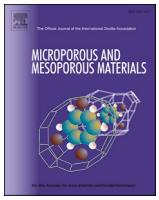

# Constructing AgY@Cu-BTC hybrid composite for enhanced sulfides capture and moisture resistance

Yang Zhao [a], Yuxiang Chen [a], Cheng Qian [a], Hao Wang [a], Hao Jiang [a], Cheng Niu [a], Junhao Gai [a], Qiyue Zhao [a], Yue Lou [a], Benxian Shen [a,b], Di Wu [c,d,e,f], Hui Sun [a,b,*], Yujun Tong [g]

[a] School of Chemical Engineering, East China University of Science and Technology, Shanghai, 200237, China
[b] International Joint Research Center of Green Energy Chemical Engineering, East China University of Science and Technology, Shanghai, 200237, China
[c] Key Laboratory of Advanced Control and Optimization for Chemical Processes, Ministry of Education, East China University of Science and Technology, Shanghai, 200237, China
[d] Alexandra Navrotsky Institute for Experimental Thermodynamics, Washington State University, Pullman, WA, 99163, United States
[e] The Gene and Linda Voiland School of Chemical Engineering and Bioengineering, Washington State University, Pullman, WA, 99163, United States
[f] Department of Chemistry, Washington State University, Pullman, WA, 99163, United States
[g] Sinopec Dalian Research Institute of Petroleum and Petrochemicals, Dalian Liaoning, 116100, China

ARTICLE INFO

*Keywords:*
Hybrid structure
Organosulfide
Adsorption
Moisture resistance

ABSTRACT

Metal-modified zeolites and function-matched metal organic frameworks (MOFs) have been adapted to different scenarios of sulfides capture in order to meet increasingly stringent quality requirements and environmental regulations. However, achieving enhanced performances of both adsorption capacity and moisture resistance is still challenging. In this study, we provided an approach to the synthesis of AgY@Cu-BTC hybrid composite for enhanced sulfides capture and moisture resistance. Multiple characterizations confirmed the hybrid structure of AgY@Cu-BTC. Additionally, computational simulation and dynamic adsorption measurement were combined to evaluate the adsorption of several typical sulfides on synthesized adsorbents, and reveal the competitive adsorption mechanism. Both Ag species and ethanol solvent lead to the partial reduction of Cu(II) to Cu(I) within the AgY@Cu-BTC framework. The dynamic adsorption capacity of the AgY@Cu-BTC is 1.54 times and 1.38 times higher than those of the parent AgY and Cu-BTC, respectively. Moreover, the AgY@Cu-BTC retains much more adsorption capability for sulfides than the AgY sample with the same water content. Present study highlights the competitive adsorption of various sulfides on the hybrid structures as well as the influences of pre-adsorbed water on sulfide adsorption, and provides insights into the function-oriented development of adsorption materials.

## 1. Introduction

Various sulfur-containing compounds including hydrogen sulfide ($H_2S$) and traces of organosulfides such as carbonyl sulfide (COS), mercaptans, and thioethers are usually contained in fossil gases (like natural gas and petroleum gases) [1]. In order to meet increasingly stringent quality requirements and environmental regulations, these harmful impurities in fuel gases should be removed efficiently [2]. Nowadays, the gas purification process is dominated by chemical absorption method employing a group of alkanolamine solvents including monoethanolamine (MEA), diethanolamine (DEA), and N-methyldiethanolamine (MDEA) [3]. Generally, these solvents show satisfactory performance for the removal of acid compounds of $H_2S$ and $CO_2$ [4], whereas fail to capture organosulfides from natural gas effectively [5]. Selective adsorption involving porous materials is an extensively used method for the removal of organosulfides from different mixtures [6,7]. A variety of adsorbents, such as synthesized zeolites [8], activated carbon (AC) [9], metal organic frameworks (MOFs) [10], and metal oxides [11], have been adapted to different scenarios of sulfides removal.

Specifically, metal-modified zeolites [12] and function-matched MOFs [13,14] have been reported as promising adsorbents for efficient capture of organosulfides. Ag-exchanged zeolite Y has shown the advantages of high capacity and selectivity for capturing organosulfide compounds including thiophene, benzothiophene, and dibenzothiophene in the model gasoline. The promising adsorption affinity to sulfides is based on both π-complexation and direct sulfide-metal (S-M)

* Corresponding author. School of Chemical Engineering, East China University of Science and Technology, Shanghai, 200237, China.
*E-mail address:* sunhui@ecust.edu.cn (H. Sun).

https://doi.org/10.1016/j.micromeso.2022.112043
Received 13 February 2022; Received in revised form 26 May 2022; Accepted 6 June 2022
Available online 10 June 2022

coordination interaction resulting from the partial overlap of electron cloud between the S atom of the sulfide molecule and the metal of the framework [15]. However, sulfide adsorption on hydrophilic framework of zeolite Y could be largely hindered by the moisture commonly coexisting in various feed gases [16,17]. Recently, a structure of copper-based metal organic framework, copper-1,3,5-benzenetricarboxylic acid (Cu-BTC), was found to exhibit promising sulfide adsorption [18,19] and its performance could be largely improved via facile structural modification [20,21]. Specifically, bromine-modified Cu-BTC has indicated the distinguished hydrophobicity and remarkable capability to capture thiophene under aqueous circumstance [22]. Additionally, Cu-BTC displays a high initial adsorption ability for *t*-butyl mercaptan (TBM) in pipeline-grade natural gas and high adsorption selectivity for TBM over other components [10]. However, the Cu-BTC framework is fragile with moisture, resulting in structural collapse under aqueous circumstance [23,24]. Although a variety of hybrid composites, including Zn-BTC/ZnO [25], ZnO@zeolite Y [26], and MOF-5@AC [27] have been attempted as the adsorption materials to optimize the capture of sulfides with respect to diverse requirements, achieving enhanced performances of both adsorption capacity and moisture resistance is still challenging.

In this work, we provided an approach toward enhanced sulfide adsorption in the presence of adsorbed water via constructing an AgY@Cu-BTC hybrid structure. The AgY@Cu-BTC composite was successfully synthesized by using AgY zeolite as the precursor in a solvothermal system. Samples were characterized applying multiple technologies including energy disperse spectroscopy (EDS), X-ray diffraction (XRD), scanning electron microscope (SEM), transmission electron microscope (TEM), $N_2$ adsorption, thermogravimetric analysis (TGA), Fourier transform infrared spectroscopy (FT-IR), Raman, and X-ray photoelectron spectroscopy (XPS). Computational simulation of adsorption equilibria and dynamic adsorption measurement in a fixed-bed were combined to carefully evaluate the adsorption of several typical sulfides on different synthesized adsorbents. Present study highlights the competitive adsorption of various sulfides on the hybrid structures as well as the influences of pre-adsorbed water on sulfide adsorption, and provides insights into the function-oriented design of adsorption materials.

## 2. Experimental methods

### 2.1. Materials and reagents

The commercial NaY in powder was obtained from Nankai University Catalysts Co., Ltd. Silver nitrate ($AgNO_3$, >99%), copper nitrate ($Cu(NO_3)_2{\cdot}3H_2O$, > 99%), and 1,3,5-benzenetricarboxylic acid ($H_3BTC$, > 98.0%) were provided by Shanghai Macklin Biochemical Co., Ltd. Ethanol (>99.5%) was purchased from Shanghai Titan Scientific Co., Ltd. Feed gas containing several sulfides (Table 1), including $H_2S$, COS, $CH_3SH$, $CS_2$, and $CH_3SCH_3$, was obtained from Shanghai Wei Chuang Standard Gas Co., Ltd. All chemicals were directly used without further purification.

**Table 1**
The composition of the feed gas.

| Component | Concentration (mg-S/m$^3$) |
|---|---|
| $H_2S$ | 511 |
| COS | 508 |
| $CH_3SH$ | 516 |
| $CS_2$ | 513 |
| $CH_3SCH_3$ | 512 |
| $CH_4$ | the rest |

### 2.2. Preparation of samples

The commercial zeolite NaY in powder was used as the starting material. AgY sample was prepared by liquid-phase ion exchange method reported in previous publications [28,29]. 5 g of NaY powder was immersed in 100 mL of 0.2 M $AgNO_3$ solution, and the mixture was stirred at 90 °C for 12 h. Then the resulting product was separated by centrifugation, washed twice, dried at 120 °C overnight, and finally calcined at 400 °C for 4 h using a muffle furnace. A Cu-BTC sample was synthesized according to previously reported process [30,31]. Using the post-synthesized AgY as a precursor, an AgY@Cu-BTC composite sample was prepared through performing a modified procedure. 0.8 g of AgY was immersed in 160 mL of ethanol solution with 0.27 M $Cu(NO_3)_2$. Another 160 mL of ethanol solution containing 0.09 M $H_3BTC$ was added into previous ethanol solution to obtain a mixture. Then the mixture was stirred for 12 h at 25 °C and the resulting AgY@Cu-BTC sample was separated by centrifugation, washed with ethanol for 3 times, dried at 85 °C for 6 h and thermally treated at 160 °C overnight. The flowchart for synthesis of AgY@Cu-BTC is presented in Fig. 1.

### 2.3. Dynamic adsorption experiment

A laboratory scale fixed-bed setup (Fig. S1) was used to evaluate the dynamic adsorption performance of several sulfides on AgY, Cu-BTC, and AgY@Cu-BTC samples. In order to improve experimental accuracy and avoid the adsorption of sulfides onto the metal material, the adsorption setup was fixed using the sulfide-proof polytetrafluoroethylene [32]. 0.3 g of adsorbent was filled into an adsorption column with inner diameter of 8 mm and height of 200 mm. All adsorption experiments were carried out at 25 °C. Prior to adsorption experiment, this system was degassed using a vacuum pump. Hereafter, the feed gas was fed at a flow rate of 84 ml/min. The outlet gas was sampled and the contents of sulfides were determined using a GC-9560 gas chromatograph (Shanghai Huaai Chromatography Analysis Co., Ltd, Shanghai, China) equipped with a flame photometric detector.

To reveal the effect of moisture on the adsorption of sulfide, the activated adsorbent samples were contacted with water vapor in a well-sealed desiccator at 40 °C for 0.5, 2, and 4 h, respectively. After that, the resulting water-adsorbing samples were used for dynamic adsorption measurement. The breakthrough adsorption capacity, $q$ (mg-S/g), is calculated using Equation (1).

$$q = [QC_0 \int_0^t (1 - \frac{C}{C_0})dt] \Big/ m \quad (1)$$

where $C_0$ and $C$ are the concentrations of sulfides in inlet and outlet gases, respectively, mg-S/m$^3$; $t$ is the sulfide breakthrough time, min; $Q$ is the flow rate of inlet gas, m$^3$/min; $m$ is the mass of adsorbent sample, g.

### 2.4. Sample characterizations

Energy disperse spectroscopy (EDS) analysis was carried out on a Falion 60 S energy dispersive spectrometer (EDAX, United States). Elemental details were collected at seven random positions to obtain the average chemical composition of each sample. X-ray diffraction (XRD) analysis was carried out on a D8X-ray diffractometer (Bruker, Germany) using Cu-Kα radiation. Data were collected in the 2θ scanning range of 5–50° with a step of 0.02°. The morphologies of samples were examined by using a NOVA Nano SEM450 scanning electron microscope (SEM; FEI, USA) with a beam current of 10 nA and an accelerating voltage of 15 kV. Transmission electron microscope (TEM) analysis was conduct on a JEOL JEM-2100 transmission electron microscope (JEOL, Japan) using an accelerating voltage of 200 kV. The surface area and pore structure of samples were analyzed using an As–6B physical adsorption analyzer

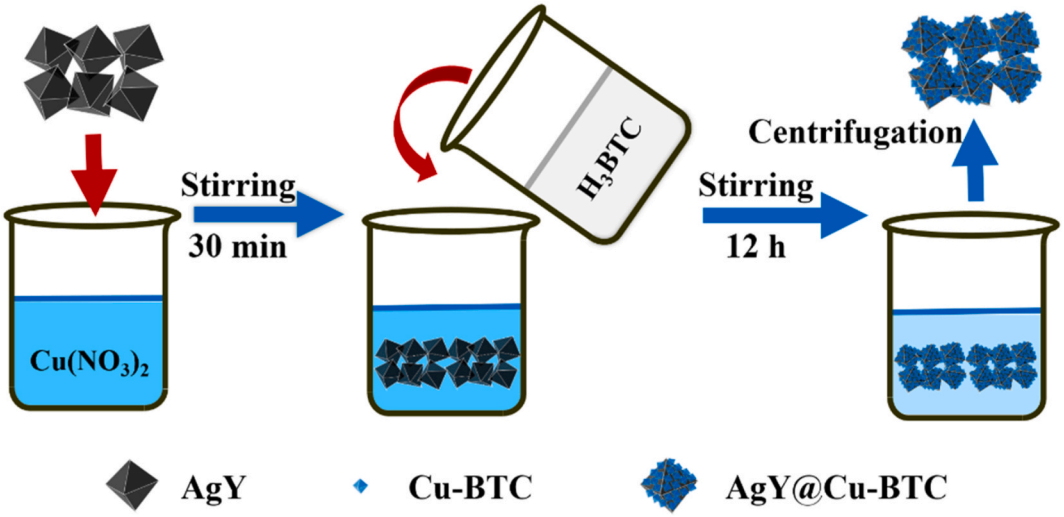


**Fig. 1.** Flowchart for synthesis of AgY@Cu-BTC.

(Qantachrom, USA). Prior to the $N_2$ adsorption test, all samples were heated to 200 °C and maintained for 2 h under vacuum level of 0.01 Pa. The specific surface area was calculated using the Brunauer-Emmett-Teller (BET) method. The pore volume was calculated by using t-Plot method. The mesopore and micropore diameters were calculated using the Barrett-Joyner-Halenda (BJH) and Horvath-Kawazoe (H–K) methods, respectively. Thermal stability of each sample was examined using a STA 449 F3 thermal gravimetric (TG) analyzer (Netzsch, Germany) under $N_2$ atmosphere. Fourier transform infrared (FT-IR) spectra were collected on a Nicolet 6700 Fourier transform spectrometer (ThermoFisher, USA) in the wavenumber range of 400–4000 $cm^{-1}$ with a resolution of 2 $cm^{-1}$. Raman spectra were obtained by using an inVia Reflex Raman spectrometer (Renishaw Plc., U.K.) with a 514 nm argon ion laser. Data were recorded from 100 to 4000 $cm^{-1}$ with a spectral resolution of 1.14 $cm^{-1}$ and a grating of 2400 lines/mm. X-ray photoelectron spectroscopy (XPS) analysis was conducted on a PHI-5300 ESCA spectrometer (PE, USA) equipped with a magnesium anode. Data were analyzed using XPS PEAK software and the contents of metals were calculated from the integration of peak areas.

### 2.5. Density functional theory (DFT) calculation

All computational simulations were performed using a Sorption module of Materials Studio 7.0 package (Accelrys Inc., USA). The sulfide adsorption on different adsorbent samples was simulated based on the grand canonical Monte Carlo (GCMC) and configurational bias methods with periodic boundary conditions [33]. The parent FAU framework topology was obtained from the Materials Studio database. Based on the compositional results obtained from the EDS analysis, the Si atoms were randomly replaced with Al atoms according to the Lowenstein's Al–O–Al avoidance rule [34]. In addition, the corresponding extra-framework ions were distributed by using the Locate task in Sorption module [35]. The structural model of Cu-BTC was obtained from the Cambridge Crystallographic Data Centre (CCDC). The framework model of AgY@Cu-BTC hybrid structure was constructed via perpendicularly stacking the unit cells of AgY and Cu-BTC on top of one another [36] (see structural models in Fig. S2). The interfacial interaction could generate between unsaturated Cu atoms of Cu-BTC framework and O atoms of zeolite FAU framework [37]. Molecular models of sulfides were established using the Sketch Atom function of the toolbar and the Clean function was used to optimize the initial molecular structure.

The adsorption isotherms of each sulfide on different structures were obtained by running the Isotherm sub-project of the Sorption module, and the temperature was fixed at 298 K. A pressure range of 0–5 kPa was used to simulate the adsorption of sulfide under low partial pressure. The obtained isotherms were fitted using the Langmuir adsorption model shown as Equation (2):

$$q_e = q_{max}\frac{bp_e}{1+bp_e} \tag{2}$$

where $q_e$ and $q_{max}$ are the adsorption capacities of monolayer adsorption at equilibrated and saturated states, mg/g. $p_e$ is the equilibrium pressure, kPa. $b$ denotes the adsorption equilibrium constant, 1/kPa. Adsorption energy for each sulfide on the unit cell of different structures was computed by using the Locate sub-project of the Sorption module. In order to prevent the influence of intermolecular interactions among absorbed sulfide molecules, the calculation was strictly restricted to the adsorption level with one sulfide molecule in each unit cell. The adsorption energy, $E_{ad}$, can be calculated using Equation (3):

$$E_{ad} = E(Z+X)\text{-}E(Z)\text{-}E(X) \tag{3}$$

where $E(Z+X)$, $E(Z)$, and $E(X)$ are the total energy of the adsorption complex, the energy of host framework and the energy of the adsorbate, respectively. Competitive adsorption of the five sulfides coexisting in a mixture on different samples is simulated by using the Fixed pressure sub-project of the Sorption module. The calculation of competitive adsorption capacity was carried out with a partial pressure of 5 kPa for each sulfide.

## 3. Results and discussion

### 3.1. Characterizations of samples

#### 3.1.1. Chemical compositions

The chemical compositions of AgY, Cu-BTC, and AgY@Cu-BTC are shown in Table 2. The characteristic elements of two parent materials are found in the AgY@Cu-BTC composite, indicating the successful synthesis of a hybrid material.

**Table 2**
Chemical compositions of synthesized samples.

| Sample | Chemical composition |
|---|---|
| AgY | $Ag_{0.056}$ $Na_{0.027}$ $Al_{0.094}$ $Si_{0.221}$ $O_{0.602}$ |
| Cu-BTC | $Cu_{0.055}$ $O_{0.302}$ $C_{0.643}$ |
| AgY@Cu-BTC | $Ag_{0.001}$ $Na_{0.010}$ $Al_{0.008}$ $Si_{0.012}$ $Cu_{0.037}$ $O_{0.275}$ $C_{0.656}$ |

### 3.1.2. XRD analysis

The XRD patterns corresponding to different samples are presented in Fig. 2. Several diffraction peaks at 2θ = 10.27°, 11.99°, 25.13°, and 25.90° are absent in the XRD pattern of AgY. In addition, the overall intensity of characteristic peaks was reduced, suggesting the probable lattice destruction during the ion-exchange or calcination process [38]. The similar ion-exchange process has been found to enable the dealumination of the FAU framework, resulting in crystallinity loss [39]. Moreover, the AgY@Cu-BTC sample show the characteristic peaks of both Cu-BTC (2θ = 6.8°, 9.6°, 11.7°, 13.6°, 15.0°, 16.6°, 17.6°, 19.3°, 20.1°, 26.1°, 29.6°, 35.4°, and 39.3°) and AgY (2θ = 6.33°, 15.76°, 18.84°, 23.78°, 27.16°, 30.89°, 31.51°, and 32.58°), indicating the hybrid framework structure of AgY@Cu-BTC [40].

Their corresponding d-spacings were listed in Table S1. The almost invisible characteristic peaks with respect to the AgY phase in the AgY@Cu-BTC composite can be explained that the AgY species located in the core exhibit less exposed crystal surface. The simulated XRD patterns are presented in Fig. S3. The simulated XRD pattern idealizes the composite material and ignore the influence of the uncleanable solvents in the actual prepared material [41], so the experimental and simulated data are not completely consistent, especially in the small angle (2θ) range of the composite material [42]. In previous studies, Fe-ZSM-5@ZIF-8 [43], ZSM-5@UIO-66-$NH_2$ [44], and Zeolite-5A@MOF-74 [45] were also found to indicate very similar co-existence of zeolite and MOF topological structures in their composites.

### 3.1.3. SEM and TEM analyses

Both SEM and TEM images of AgY, Cu-BTC, and AgY@Cu-BTC are shown in Fig. 3. From the SEM and TEM morphologies, AgY exhibits a regular octahedron crystal structure and crystal size of 300–500 nm while Cu-BTC shows an irregular crystal structure with crystal size of 100–500 nm. Present crystal morphology of Cu-BTC is quite different from the octahedral structure synthesized through a typical solvothermal method [46]. Moreover, it is clearly indicated that the AgY crystals are covered with Cu-BTC nano particles having a smaller size of about 20 nm in average. This can be explained that the surface of the zeolite particles can act as nucleation sites to produce a large number of nuclei. Moreover, there is significant effect of steric hindrance of the surrounding, which prolongs the growth of Cu-BTC crystals on the AgY surface [47]. Both SEM and TEM results indicate that the parent AgY crystals are wrapped by Cu-BTC nano crystals to form the hybrid structure of AgY@Cu-BTC composite. We also present the SEM images of samples collected at different reaction temperatures (see Fig. S4). It is indicated that these composite samples have consistent particle size with the parent AgY. Fig. S4 (a) shows the morphology of a sample obtained from an unsuccessfully synthesis, indicating the rare AgY particles without coating of Cu-BTC particles. Overall, the synthesized composite samples have heterogeneous crystal structure and maintain the architecture and size of AgY particles. Moreover, the SEM image of Cu-BTC sample indicates that a synthesis system without involving the AgY particles will result in a completely different product, containing only particles without coating of nanosized species. In general, it is hard to form a hybrid crystalline structure (like a coating one) with a homogenous phase composition. However, we have realized that our AgY@Cu-BTC composite has an incompletely encapsulated core-shell structure, which is very similar to Fe-ZSM-5@ZIF-8, MOR/MIL-101, and ZSM-5@UIO-66-$NH_2$ reported by Imyen [43], Fallah [48], and Zhu [44], rather than Zeo-A@MOF-74 reported by Naddaf [45].

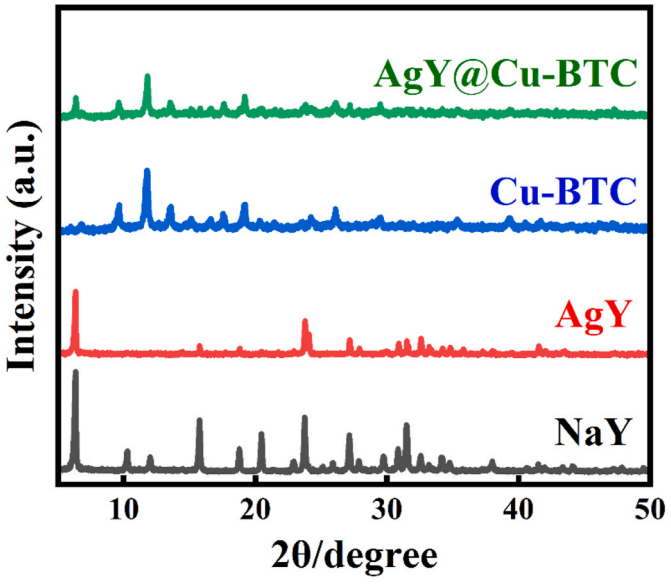


**Fig. 2.** XRD patterns of NaY, AgY, Cu-BTC, and AgY@Cu-BTC.

### 3.1.4. XPS characterization

To reveal the binding state of metals involved in different samples, XPS characterizations were conducted on AgY, Cu-BTC, and AgY@Cu-BTC and the XPS patterns are presented in Fig. 4. All binding energies were corrected by taking the C 1s peak at 284.6 eV as a reference. A peak located at 369.0 eV (Fig. 4 (a) and (c)) is assigned to Ag $3d_{5/2}$, confirming the form of $Ag^+$ in both AgY and AgY@Cu-BTC structures [49]. By integrating the XPS peaks at 374.8 and 369.0 eV, associated with Ag $3d_{3/2}$ and Ag $3d_{5/2}$, we can conclude that AgY@Cu-BTC has lower Ag content than AgY, which is accordance with our previous results of composition measurement. In addition, AgY@Cu-BTC displays an additional Cu(I) $2p_{3/2}$ peak at 932.8 eV, resulting from the reduction of Cu(II) in presence of ethanol and Ag species. The ethanol solvent and the Ag species from AgY play the roles of reducing agent and catalyst respectively, which enable the conversion of Cu(II) to Cu(I) during the solvothermal synthesis [23]. The molar ratio of Cu(II) to Cu(I) is found to be of 3.02.

### 3.1.5. FT-IR and Raman analyses

FT-IR and Raman analyses were carried out to examine the structural details of AgY, Cu-BTC, and AgY@Cu-BTC (Fig. S5). In the FT-IR spectrum of AgY, the vibrations at 460, 720, and 1040 $cm^{-1}$ are assigned to T-O bond of $TO_4$ tetrahedron of FAU framework [50]. Moreover, the vibrations located at 580, 790, and 1160 $cm^{-1}$ are designated to the double six-membered ring (D6R) [51]. In addition, the bands at 3450 and 1630 $cm^{-1}$ can be assigned to the free or coordinated hydroxyl groups [52,53]. Two Raman bands at 503 $cm^{-1}$ and 298 $cm^{-1}$ can be assigned to the vibrations of the four-membered ring (4R) and D6R of the FAU framework [53]. In case of the FT-IR spectrum of Cu-BTC, the band at 1630 $cm^{-1}$ is assigned to the symmetric stretching vibration of the carboxylate group, while the bands at 1442.3 and 1372.9 $cm^{-1}$ correspond to the asymmetric stretching vibration [54]. The same absorption peak at 3450 $cm^{-1}$ is also designated to the –OH stretching vibration caused by the incomplete removal of water or ethanol solvent [55]. Raman spectrum indicates a typical absorption mode of Cu-BTC, including the asymmetric stretching vibrations of benzene ring at both 1614 $cm^{-1}$ and 1004 $cm^{-1}$ [56], the O–C–O asymmetric and symmetric stretching vibrations at 1543 $cm^{-1}$ and 1460 $cm^{-1}$, the Cu(II)–O vibrations relating to the carboxylic acid bridge at 275 $cm^{-1}$, 480 $cm^{-1}$, and 503 $cm^{-1}$ [57], and the Cu–Cu stretching vibration at 170-195 $cm^{-1}$. As for the AgY@Cu-BTC composite sample, its FT-IR spectrum exhibits the characteristic absorption peaks of both AgY and Cu-BTC frameworks, confirming the hybrid structure of AgY and Cu-BTC. Furthermore, the AgY@Cu-BTC composite shows weaker peak intensity than the AgY sample but much stronger peak intensity as compared to the Cu-BTC sample. In the Raman spectrum of AgY@Cu-BTC, the absorption peaks at 1614 and 1543 $cm^{-1}$ are found to become broader and merge together. Moreover, three peaks at 175, 270,

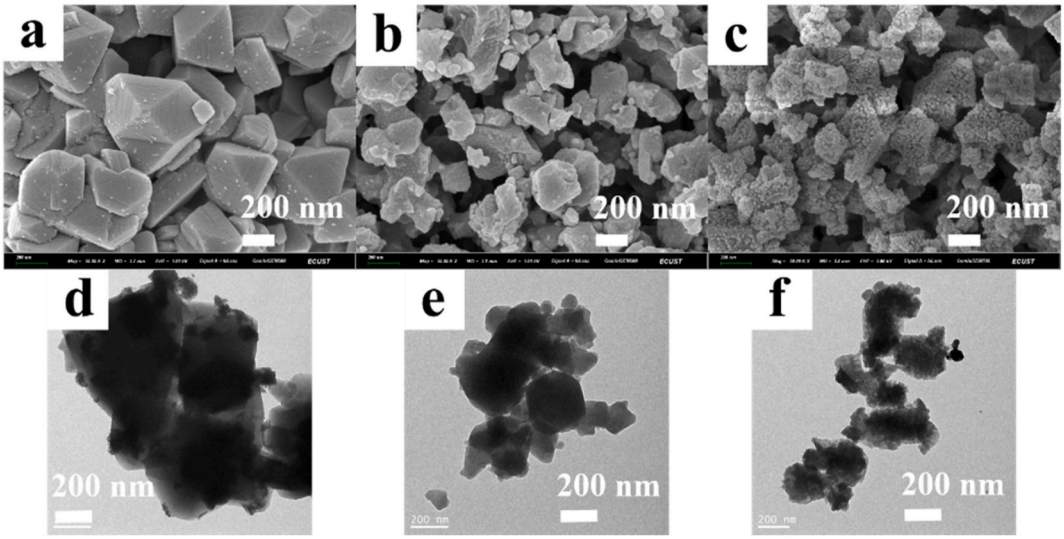


**Fig. 3.** SEM images of **(a)** AgY, **(b)** Cu-BTC, **(c)** AgY@Cu-BTC, and TEM images of **(d)** AgY, **(e)** Cu-BTC, **(f)** AgY@Cu-BTC.

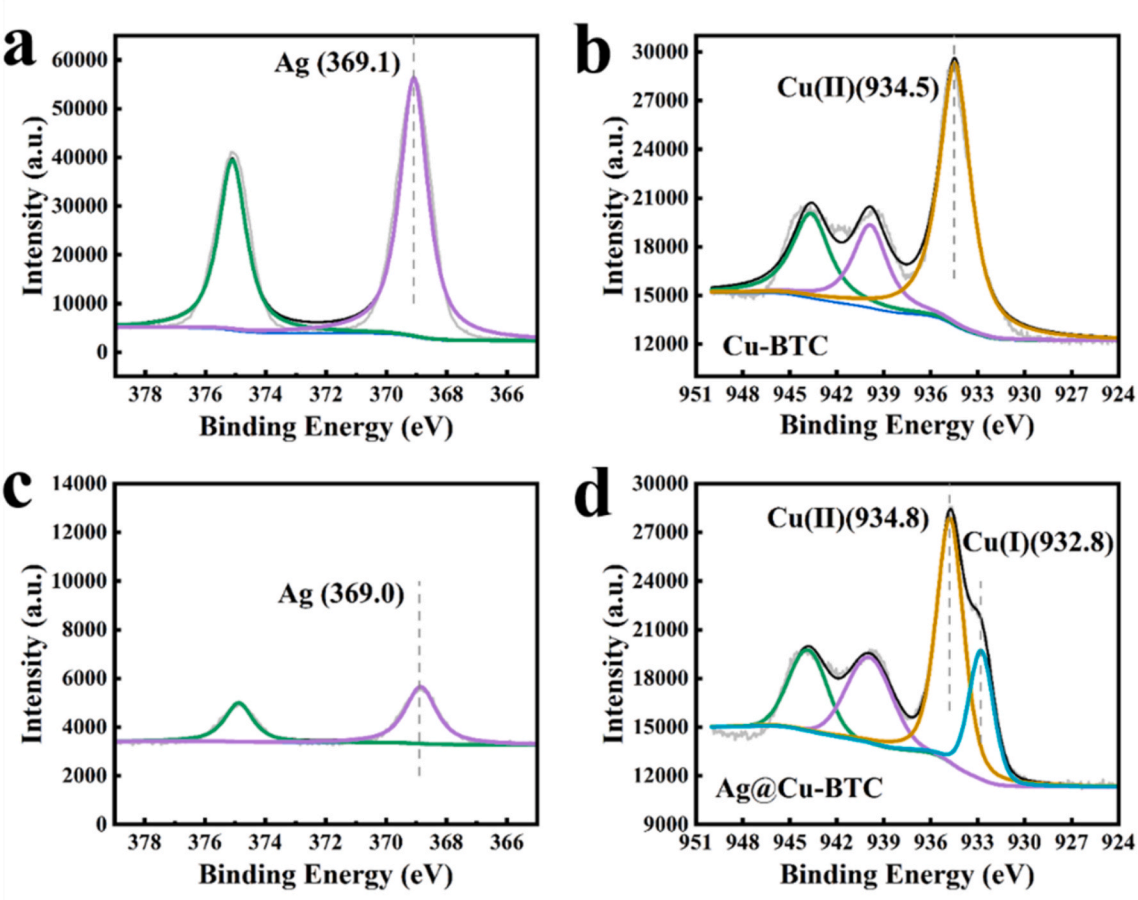


**Fig. 4.** Ag 3d XPS spectra of **(a)** AgY, **(c)** AgY@Cu-BTC, and Cu 2p XPS spectra of **(b)** Cu-BTC and **(d)** AgY@Cu-BTC.

and 480 $cm^{-1}$ become weaker or even disappear. Specifically, the reduced peak intensity of 173 $cm^{-1}$ indicates that the Cu–Cu bond in the framework structure is weakened. The absence of two peaks at 275 $cm^{-1}$ and 503 $cm^{-1}$ suggests the breakage of Cu(II)–O bond resulting from the reduction of Cu(II) to Cu(I) in the framework [58]. All these spectral changes can be ascribed to the structure evolution of AgY@Cu-BTC during the synthesis process, which are in accordance with the damped XRD intensity. Additionally, two additional peaks at 233 and 945 $cm^{-1}$, which are responsible for the Cu(I)–$O_{0.5}$ vibration [59], can be clearly recognized in the spectrum of AgY@Cu-BTC, confirming the existence of Cu(I). However, the Ag–O stretching vibration is not detectable because of the extremely low content of Ag in the synthesized sample [60].

### 3.1.6. $N_2$ adsorption

$N_2$ adsorption measurements were performed to figure out the pore structures of different synthesized samples. From the $N_2$ adsorption-desorption isotherms illustrated in Fig. S6 (a), both Cu-BTC and AgY@Cu-BTC show type-IV adsorption isotherms. The hysteresis loops in the relative pressure ranging from 0.8 to 1.0 indicate that both of them have hierarchical pore structures [61,62]. According to the calculated results (see Table S2), as compared to the AgY sample, the AgY@Cu-BTC sample shows reduced micropore volume but largely improved total pore volume owing to the contribution of mesoporous structure of Cu-BTC or interparticle pores of two-phase materials. From the pore size distributions (Fig. S6 (b)), AgY has a BJH average pore diameter of 4.4 nm while Cu-BTC and AgY@Cu-BTC have the average pore size of 16.0 nm and 16.3 nm, respectively. Meanwhile, the HK micropore diameter of AgY is of 0.658 nm while those of Cu-BTC and AgY@Cu-BTC are found to be 0.683 nm and 0.662 nm, respectively.

### 3.1.7. TG analysis

Thermogravimetric analyses were performed on the AgY, Cu-BTC, and AgY@Cu-BTC samples to examine their thermal stability. All TG traces (Fig. S7) show an initial weight loss in the temperature range of 30–150 °C, which is attributed to the removal of adsorbed impurities (including moisture and residual solvent). As the temperature continues to rise, AgY zeolite shows no further mass loss, whereas both Cu-BTC and AgY@Cu-BTC exhibit a sharp weight loss at around 320 °C, corresponding to the structural collapse of organic frameworks [63].

## 3.2. Adsorption equilibria of sulfides on different samples

The simulated adsorption isotherms of sulfides on AgY, Cu-BTC, AgY@Cu-BTC are shown in Fig. 5. The Langmuir model was used to fit all adsorption isotherms and the observed model parameters are listed in Table S3. The saturated adsorption capacities, $q_{max}$, for $H_2S$, COS, $CH_3SH$, $CS_2$, $CH_3SCH_3$ on AgY are found to be 84.61, 35.30, 91.86, 55.37, and 153.82 mg/g, respectively. This ranking order can be explained by the S-M interactions which dominate the adsorption affinity to these sulfide compounds [64–66]. The stronger guest-host interactions can endow the adsorbent with the greater adsorption affinity to sulfides. According to the fitted Langmuir adsorption equilibrium constants, the adsorption degrees of sulfides on AgY rank the order: $H_2S$ > $CS_2$ > COS > $CH_3SH$ > $CH_3SCH_3$. From Table S3, the Cu-BTC has the $q_{max}$ of 494.43 mg/g for $H_2S$, 110.71 mg/g for COS, 335.93 mg/g for $CH_3SH$, 176.13 mg/g for $CS_2$, and 234.13 mg/g for $CH_3SCH_3$, which are much higher than those of AgY. As for the AgY@Cu-BTC hybrid composite, these sulfides have either higher saturated adsorption capacities (272.74 mg/g vs. 234.13 mg/g for $CH_3SCH_3$) or higher adsorption equilibrium constants (0.84 vs. 0.07 for $H_2S$, 4.11 vs. 0.04 for COS, 2.69 vs. 1.36 for $CH_3SH$, and 3.09 vs. 0.34 for $CS_2$) as compared to their adsorption on Cu-BTC sample, indicating the coupled advantages of the parent AgY and Cu-BTC. Meanwhile, the simulated adsorption energies for five sulfides on AgY, Cu-BTC, and AgY@Cu-BTC are shown in Fig. 6. Among three adsorbents, all sulfides except COS show the most exothermic adsorption energies on the hybrid AgY@Cu-BTC. Additionally, in all adsorbent cases, the adsorption energies for these sulfides are in the consistent sequence with their saturated adsorption capacities. It can be concluded that sulfides having stronger interaction with the host frameworks exhibit higher adsorption affinity. This conclusion can also be supported by the competitive adsorption capacities simulated via using a mixed feed containing these sulfides simultaneously (Fig. S8).

The interactions between metal adsorption sites of the frameworks and the sulfide molecules are confirmed to dominate the adsorption of sulfides on adsorbents. Our previous evidence strongly suggests the complex integration of increased binding site affinity from Cu(I) and more open pore structure prior to pore collapse, which leads to the sulfide uptake boost on Cu(I)-containing Cu-BTC. In addition, such enhancement in adsorption capacity can also be attributed to the interfacial structure of the two-phase structure as well as the synergistic effect of the hybrid composite. The adsorption capacities of various materials reported in earlier publications are summarized in Table S4. These metal-exchanged zeolites show their adsorption capacities of 0.060–64.8 mg-S/g for sulfides (i.e., $H_2S$, COS, $CH_3SH$, $CS_2$, and $CH_3SCH_3$) contained in natural gas [6,8,65,66]. The adsorption capacity of modified ZSM-5 [67] and Y [39] zeolite for DMDS is less than 40 mg-S/g. In addition, the adsorption capacity of $H_2S$ on ZnBTC/ZnO is found to be of 14.2 mg-S/g [25], and the capacity of thiophene on MOF-5@AC is 11.34 mg-S/g [27]. In comparison, the AgY@Cu-BTC shows large advantage of sulfide capture.

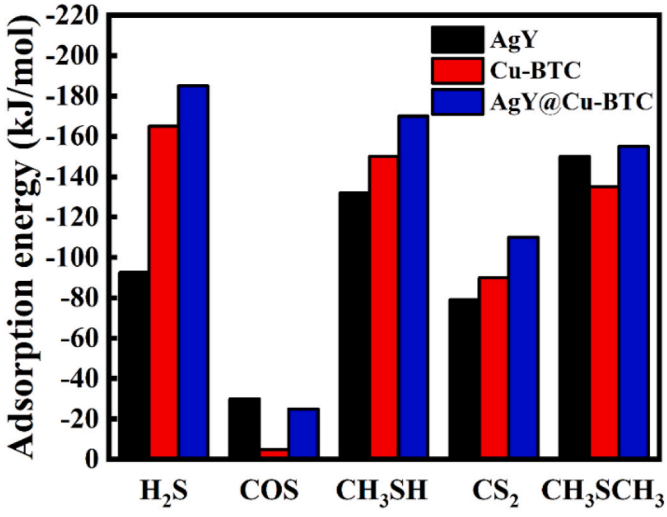


**Fig. 6.** Adsorption energies for five sulfides on AgY, Cu-BTC, and AgY@Cu-BTC.

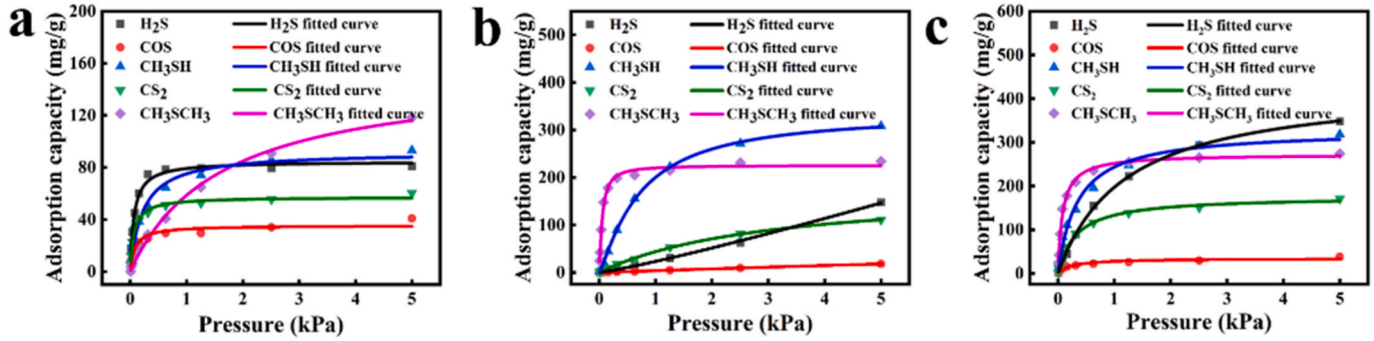


**Fig. 5.** Adsorption isotherms for sulfides on **(a)** AgY, **(b)** Cu-BTC, and **(c)** AgY@Cu-BTC.

### 3.3. Dynamic adsorption tests

Dynamic adsorption experiments were carried out in fixed-bed filled with AgY, Cu-BTC, and AgY@Cu-BTC. The adsorption breakthrough curves for five sulfides are demonstrated in Fig. 7. Different sulfides show distinct adsorption breakthrough times. As for the AgY adsorbent, COS shows the shortest adsorption breakthrough time of around 60 min. Hereafter, $CS_2$, $H_2S$, and $CH_3SH$ can been detected in sequence at 90 min, 150 min, and 170 min, respectively. $CH_3SCH_3$ has the longest breakthrough time of 300 min. Using Cu-BTC as an adsorbent, these sulfides rank a quite different order of dynamic adsorption. Although the first detectable component is still COS, Cu-BTC shows barely adsorption affinity to COS. Following COS, $CS_2$ shows a breakthrough time of 120 min. In addition, $CH_3SCH_3$, $CH_3SH$, and $H_2S$ exhibit the breakthrough times of 230, 240, and 250 min, respectively. The adsorption breakthrough of the AgY@Cu-BTC bed is in the same sequence to that of the Cu-BTC bed. The breakthrough times are found to be 50 min for COS, 140 min for $CS_2$, 240 min for $CH_3SCH_3$, 300 min for $CH_3SH$, and 360 min for $H_2S$, respectively. It is worth noting that all sulfides except for the one having the longest breakthrough time (i.e., $CH_3SCH_3$ for AgY as well as $H_2S$ for both Cu-BTC and AgY@Cu-BTC) display the maximum relative concentrations $C/C_0 > 1$. It means that the outlet concentrations are higher than their original contents in the feed gas, indicating the adsorption displacement among these sulfides under a competitive adsorption scenario. As a result, it can be informed that the adsorption of sulfides on all samples is at least partially reversible. Furthermore, the earlier breakthrough components have much weaker adsorption affinity as compared with the components having longer breakthrough times, leading to their partial displacement by the later ones [68]. The breakthrough adsorption capacities for five sulfides on AgY, Cu-BTC, and AgY@Cu-BTC calculated from the adsorption breakthrough curves are presented in Fig. 8. AgY, Cu-BTC, and AgY@Cu-BTC have the total adsorption capacities of 67 mg/g, 75 mg/g, and 104 mg/g, respectively. The total adsorption capacity of the hybrid AgY@Cu-BTC is 1.54 times and 1.38 times higher than those of the parent AgY and Cu-BTC.

### 3.4. Effect of water content on adsorption of sulfides

A series of AgY@Cu-BTC samples with water contents of 0.07, 0.32, and 0.4 g/g were filled into the fixed-bed to evaluate the influences of water content on dynamic adsorption of sulfides on the hybrid adsorbent. AgY samples with water contents of 0.06, 0.28, and 0.32 g/g were also measured for comparison. The obtained adsorption breakthrough curves and the calculated breakthrough adsorption capacities are shown in Figs. 9 and 10, respectively. The adsorption displacement still occurs during the dynamic adsorption on water-contained adsorbents. With the increase of water uptake, all sulfides show decreasing breakthrough times as well as descending adsorption capacities. Specifically, the dynamic adsorption capacities of these samples with water contents of 0.06, 0.28, and 0.32 g/g are reduced by 31.4%, 58.8%, and 63.6%,

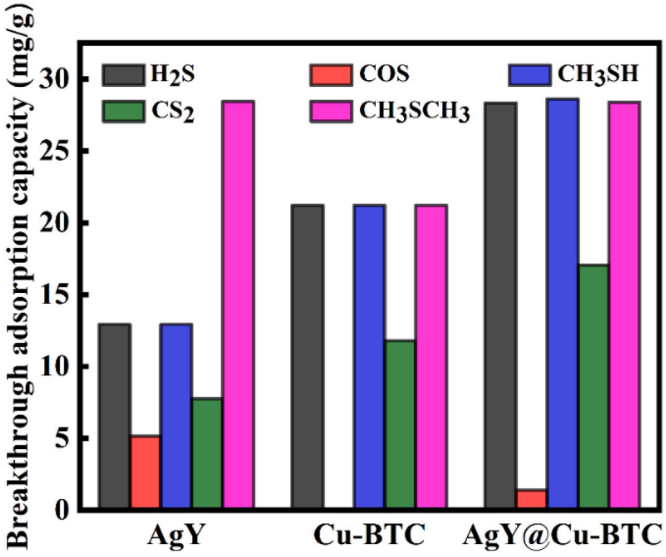


**Fig. 8.** Breakthrough adsorption capacities for five sulfides on AgY, Cu-BTC, and AgY@Cu-BTC.

respectively. In the presence of moisture, a part of active adsorption sites in the adsorbent are preferentially saturated with polar water molecules. Besides, diffusion of sulfides can also be hindered by the pre-adsorbed water molecules in diverse adsorbents [69]. The combined effects lead to the largely reduced dynamic adsorption capacities for sulfides.

Compared with the anhydrous AgY@Cu-BTC sample, three hybrid samples with water contents of 0.07, 0.32, and 0.4 g/g exhibit the capacity loss of 10.3%, 28.6%, and 39.3%, respectively. According to the study reported by Yu et al. [22], the adsorption capacity of thiophene on Cu-BTC samples with pre-adsorbed water of 0.03 and 0.06 g/g were reduced by about 34% and more than 91%. At the same level of water content, the AgY@Cu-BTC hybrid structure retains much more adsorption capability for sulfides. It can be concluded that the wrapped structure of AgY by Cu-BTC in the composite can increase the moisture resistance and, therefore, reduce the negative effect of the presence of moisture on the adsorption of sulfides.

## 4. Conclusions

In this study, a AgY@Cu-BTC hybrid composite was successfully synthesized by using AgY zeolite as the precursor in a solvothermal system. Combined characterizations confirm that the AgY@Cu-BTC composite has a hybrid structure with the parent AgY crystal wrapped by Cu-BTC nano crystals. In addition, both ethanol solvent and Ag species from the AgY enable the partial reduction of Cu(II) to Cu(I) within the AgY@Cu-BTC framework through acting as reducing agent

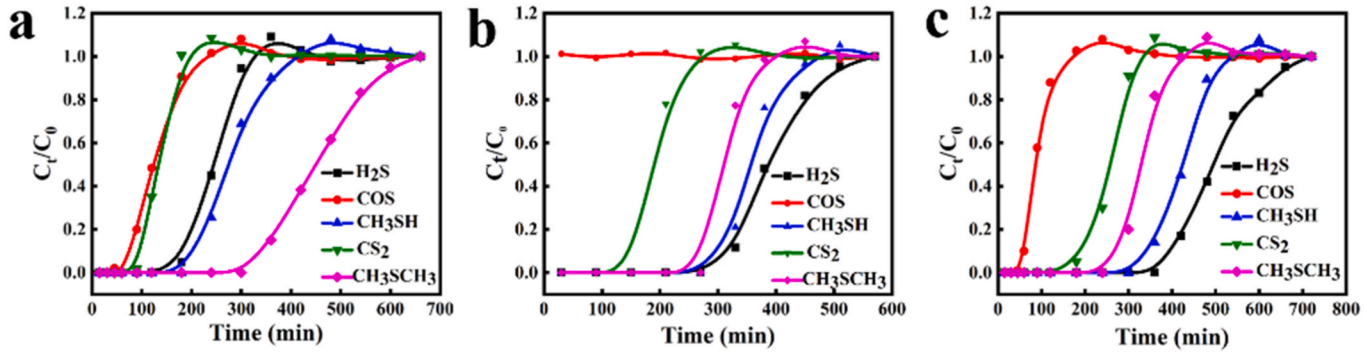


**Fig. 7.** Adsorption breakthrough curves for five sulfides on fixed-bed filled with **(a)** AgY **(b)** Cu-BTC, and **(c)** AgY@Cu-BTC.

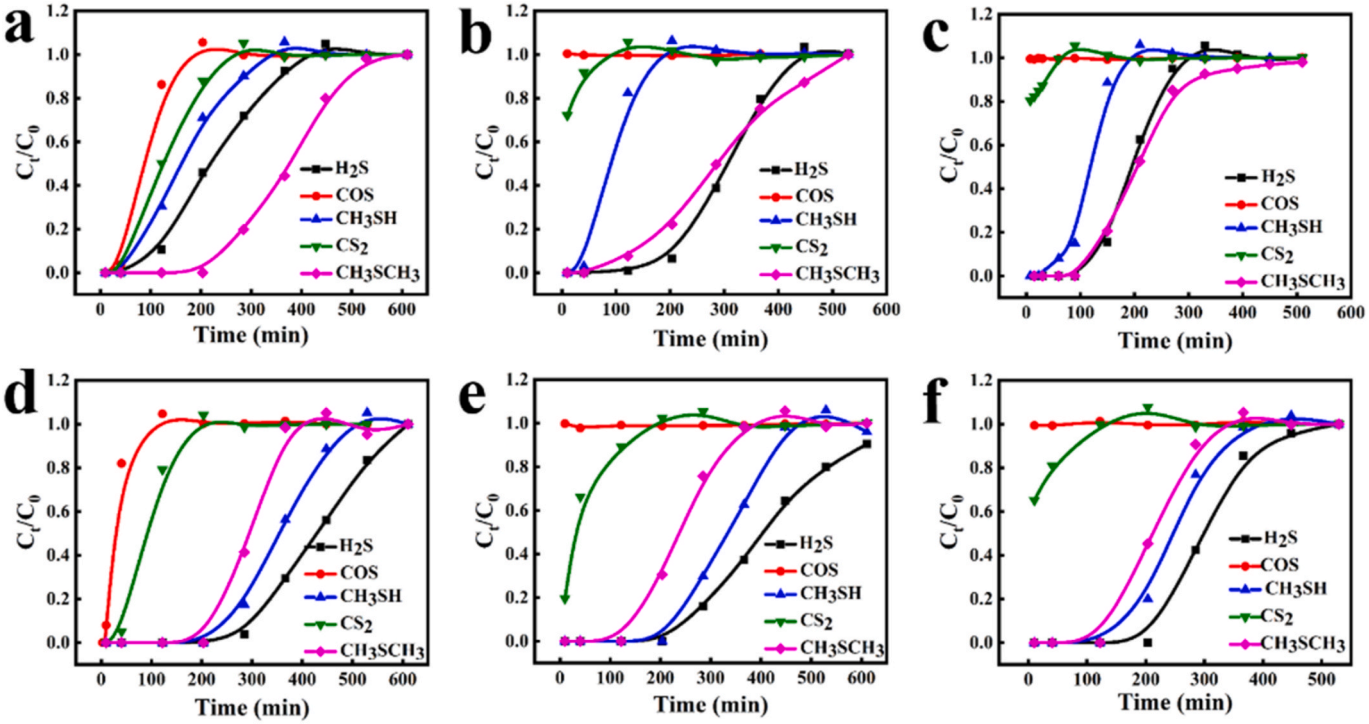


**Fig. 9.** Adsorption breakthrough curves of AgY with water contents of **(a)** 0.06, **(b)** 0.28, **(c)** 0.32 g/g, and AgY@Cu-BTC with water contents of **(d)** 0.07, **(e)** 0.32, **(f)** 0.4 g/g.

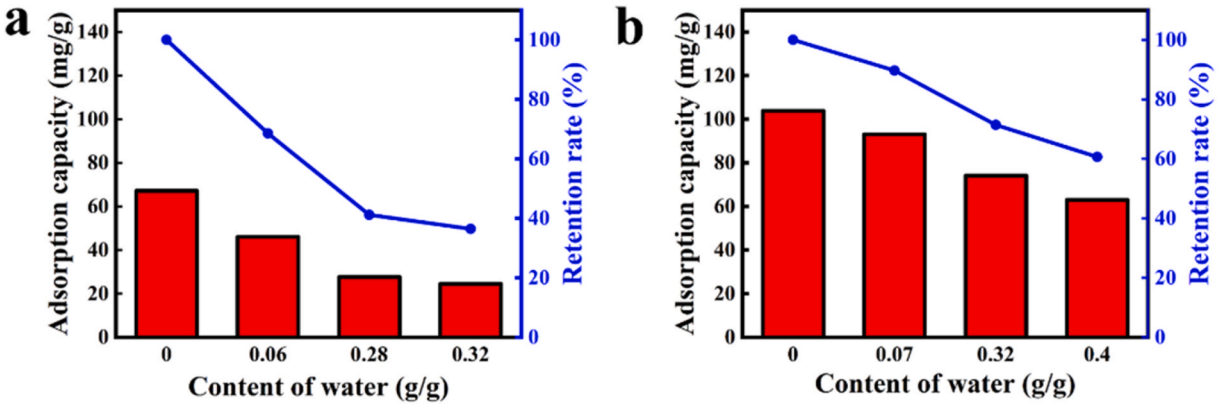


**Fig. 10.** Breakthrough adsorption capacity of **(a)** AgY and **(b)** AgY@Cu-BTC with different water contents.

and catalyst, respectively. The AgY@Cu-BTC sample has either higher saturated capacities or higher equilibrium constants for sulfide adsorption than the Cu-BTC sample. As compared to the adsorption on AgY and Cu-BTC, all sulfides except COS show more exothermic energies of adsorption on the AgY@Cu-BTC. Meanwhile, the breakthrough adsorption capacity of the AgY@Cu-BTC is 1.54 times and 1.38 times higher than those of the AgY and Cu-BTC, respectively. Moreover, the AgY@Cu-BTC retains much more adsorption capability for sulfides than AgY sample having the same water content. The enhanced adsorption capacity of the AgY@Cu-BTC can be attributed to the interfacial structure of two parent frameworks as well as the synergistic effect of the hybrid composite. Furthermore, the hybrid structure can be beneficial to the moisture resistance and, therefore, reduce the negative effect of the presence of moisture on the adsorption of sulfides.

## CRediT authorship contribution statement

**Yang Zhao:** Writing – original draft, Resources, Investigation. **Yuxiang Chen:** Writing – review & editing, Validation. **Cheng Qian:** Data curation. **Hao Wang:** Investigation. **Hao Jiang:** Formal analysis. **Cheng Niu:** Validation. **Junhao Gai:** Methodology. **Qiyue Zhao:** Investigation. **Yue Lou:** Methodology. **Benxian Shen:** Conceptualization. **Di Wu:** Conceptualization. **Hui Sun:** Writing – review & editing, Supervision, Investigation, Conceptualization. **Yujun Tong:** Methodology.

## Declaration of competing interest

The authors declare that they have no known competing financial interests or personal relationships that could have appeared to influence the work reported in this paper.

## Acknowledgments

This work is financially supported by the National Natural Science Foundation of China (Grant21878097 and 22178109) and the Natural

Science Foundation of Shanghai (Grant 21ZR1417700). D.W. acknowledges the institutional funds from the Gene and Linda Voiland School of Chemical Engineering and Bioengineering, and the Alexandra Navrotsky Institute for Experimental Thermodynamics at Washington State University.

## Appendix A. Supplementary data

Supplementary data to this article can be found online at https://doi.org/10.1016/j.micromeso.2022.112043.

## References

[1] S.Z. Zhao, H.H. Yi, X.L. Tang, F.Y. Gao, B.W. Zhang, Z.X. Wang, Y.R. Zuo, Methyl mercaptan removal from gas streams using metal-modified activated carbon, J. Clean. Prod. 87 (2015) 856–861, https://doi.org/10.1016/j.jclepro.2014.10.001.

[2] C. Xu, G.T. Xu, B.N. Zong, Z.K. Xie, Analytical progress of trace impurities in hydrogen for fuel cell vehicles, Chem. Ind. Eng. Prog. 40 (2021) 688–702, https://doi.org/10.16085/j.issn.1000-6613.2020-0690.

[3] R.T. Rodrigo, B. Chakib, Reaction kinetics of carbonyl sulfide (COS) with diethanolamine in methanolic solutions, Ind. Eng. Chem. Res. 47 (2008) 7375–7380, https://doi.org/10.1021/ie8002649.

[4] J.A. Awan, G.M. Kontogeorgis, I. Tsivintzelis, C. Coquelet, Vapor-liquid-liquid equilibrium measurements and modeling of ethanethiol methane water, 1-propanethiol methane water and 1-butanethiol methane water ternary systems at 303, 335, and 365 K and pressure up to 9 MPa, Ind. Eng. Chem. Res. 52 (2013) 14698–14705, https://doi.org/10.1021/ie400779m.

[5] F. Zhang, B.X. Shen, H. Sun, J.C. Liu, L. Liu, Rational formulation design and commercial application of a new hybrid solvent for selectively removing $H_2S$ and organosulfurs from sour natural gas, Energy Fuel. 30 (2016) 12–19, https://doi.org/10.1021/acs.energyfuels.5b02214.

[6] X. Chen, B.X. Shen, H. Sun, G.X. Zhan, Ion-exchange modified zeolites X for selective adsorption desulfurization from Claus tail gas: experimental and computational investigations, Microporous Mesoporous Mater. 261 (2018) 227–236, https://doi.org/10.1016/j.micromeso.2017.11.014.

[7] X. Peng, D.P. Cao, Computational screening of porous carbons, zeolites, and metal organic frameworks for desulfurization and decarburization of biogas, natural gas, and flue gas, AIChE J. 59 (2013) 2918–2942, https://doi.org/10.1002/aic.14046.

[8] L.J. Zhu, X.F. Lv, S.Y. Tong, T.T. Zhang, Y.R. Song, Y.J. Wang, Z. Hao, C. Huang, D. H. Xia, Modification of zeolite by metal and adsorption desulfurization of organic sulfide in natural gas, J. Nat. Gas Sci. Eng. 69 (2019) 102941–102950, https://doi.org/10.1016/j.jngse.2019.102941.

[9] Q. Juan, P. Ning, X.Q. Wang, K. Li, W. Liu, W. Chen, L.L. Wang, Removing carbonyl sulfide with metal-modified activated carbon, Front. Chem. Sci. Eng. 1 (2016) 11–18, https://doi.org/10.1007/s11783-014-0714-5.

[10] G. Chen, S. Tan, W.J. Koros, C.W. Jones, Metal organic frameworks for selective adsorption of t-butyl mercaptan from natural gas, Energy Fuel. 29 (2015) 3312–3321, https://doi.org/10.1021/acs.energyfuels.5b00305.

[11] L.F. Wang, R. Yang, New nanostructured sorbents for desulfurization of natural gas, Front. Chem. Sci. Eng. 8 (2014) 8–19, https://doi.org/10.1007/s11705-014-1411-4.

[12] S.Y. Jung, J.M. Moon, S.C. Lee, S.C. Paik, K.S. Park, J.C. Kim, The adsorption properties of organic sulfur compounds on zeolite-based sorbents impregnated with rare-earth metals, Adsorption 20 (2014) 341–348, https://doi.org/10.1007/s10450-013-9597-1.

[13] K. Yang, Y. Yan, W. Chen, H.T. Kang, Y. Han, W.Q. Zhang, Y.F. Fan, Z.X. Li, The high performance and mechanism of metal-organic frameworks and their composites in adsorptive desulfurization, Polyhedron 152 (2018) 202–215, https://doi.org/10.1016/j.poly.2018.06.036.

[14] Z.P. Chen, L.X. Ling, B.J. Wang, H.L. Fan, S.G. Ju, J. Mi, Adsorptive desulfurization with metal-organic frameworks: a density functional theory investigation, Appl. Surf. Sci. 387 (2016) 483–490, https://doi.org/10.1016/j.apsusc.2016.06.078.

[15] H. Song, X.H. Cui, H.L. Song, H.J. Gao, F. Li, Characteristic and adsorption desulfurization performance of Ag-Ce bimetal ion-exchanged Y zeolite, Ind. Eng. Chem. Res. 53 (2014) 14552–14557, https://doi.org/10.1021/ie404362f.

[16] X.J. Liu, D.Z. Yi, Y.Y. Cui, L. Shi, X. Meng, Adsorption desulfurization and weak competitive behavior from 1-hexene over cesium-exchanged Y zeolites (CsY), J. Eng. Chem. 27 (2018) 271–277, https://doi.org/10.1016/j.jechem.2017.04.006.

[17] Y.X. Li, J.X. Shen, S.S. Peng, J.K. Zhang, J. Wu, X.Q. Liu, L.B. Sun, Enhancing oxidation resistance of Cu(I) by tailoring microenvironment in zeolites for efficient adsorptive desulfurization, Nat. Commun. 11 (2020) 3206–3215, https://doi.org/10.1038/s41467-020-17042-6.

[18] L.M. Wu, J. Xiao, Y. Wu, S.k. Xian, G. Miao, H.H. Wang, Z. Li, A combined experimental/computational study on the adsorption of organosulfur compounds over metal-organic frameworks from fuels, Langmuir 30 (2014) 1080–1088, https://doi.org/10.1021/la404540j.

[19] Y. Li, L.J. Wang, H.L. Fan, S.G. Ju, H. Wang, J. Mi, Removal of sulfur compounds by a copper-based metal organic framework under ambient conditions, Energy Fuel. 29 (2015) 298–304. https://doi.org/10.1021/ef501918f.

[20] Y.X. Chen, D. Wang, H. Jiang, J.L. Tan, Y. An, Y.H. Chen, Y. Wu, H. Sun, B.X. Shen, J.G. Zhao, J.C. Liu, H. Ling, D. Wu, X. Han, S.X. Xu, Structure-property-energetics relationship of organosulfide capture using Cu(I)/Cu(II)-BTC edited by valence engineering, Ind. Eng. Chem. Res. 60 (2021) 371–377, https://doi.org/10.1021/acs.iecr.0c05483.

[21] S. Ban, K.Y. Long, J. Xie, H. Sun, H.J. Zhou, Thiophene separation with silver-doped Cu-BTC metal-organic framework for deep desulfurization, Ind. Eng. Chem. Res. 57 (2018) 2956–2966, https://doi.org/10.1021/acs.iecr.7b04496.

[22] L. Yu, Q. Liu, W. Dai, N. Tian, N. Ma, Efficient thiophene capture with a hydrophobic Cu-BTC-(n)Br adsorbent in the presence of moisture, Microporous Mesoporous Mater. 266 (2018) 7–13, https://doi.org/10.1016/j.micromeso.2018.02.032.

[23] H. Sun, X. Han, K.F. Liu, B.X. Shen, J.C. Liu, D. Wu, X.Y. Shi, Metal-modified Cu-BTC for highly-enhanced adsorption of organosulfur specie, Ind. Eng. Chem. Res. 56 (2017) 9541–9550, https://doi.org/10.1021/acs.iecr.7b02392.

[24] Y.P. Guo, W. Xie, H. Li, J.P. Li, J. Hu, H.L. Liu, Construction of hydrophobic channels on Cu(I)-MOF surface to improve selective adsorption desulfurization performance in presence of water, Separ. Purif. Technol. 285 (2022), https://doi.org/10.1016/j.seppur.2021.120287.

[25] N.K. Gupta, J. Bae, S. Kim, K.S. Kim, Fabrication of Zn-MOF/ZnO nanocomposites for room temperature $H_2S$ removal: adsorption, regeneration, and mechanism, Chemosphere 274 (2021) 129789–129800, https://doi.org/10.1016/j.chemosphere.2021.129789.

[26] Y. Yang, S. Mandizadeh, H. Zhang, S.N. Masoud, The role of ZnO in reactive desulfurization of diesel over ZnO@Zeolite Y: classification, preparation, and evaluation, Separ. Purif. Technol. 256 (2021) 117784–117794, https://doi.org/10.1016/j.seppur.2020.117784.

[27] L.J. Zhu, X.Y. Jia, H. Bian, T. Huo, Z.B. Duan, Y.Z. Xiang, D.H. Xia, Structure and adsorptive desulfurization performance of the composite material MOF-5@AC, New J. Chem. 42 (2018) 3840–3850, https://doi.org/10.1039/C7NJ04192F.

[28] M.L.M. Oliveira, A.A.L. Miranda, C.M.B.M. Barbosa, C.L. Cavalcante, D.C. S. Azevedo, R.C. E, Adsorption of thiophene and toluene on NaY zeolites exchanged with Ag(I), Ni(II) and Zn(II), Fuel 88 (2009) 1885–1892, https://doi.org/10.1016/j.fuel.2009.04.011.

[29] D.L. King, L.Y. Li, Removal of sulfur components from low sulfur gasoline using copper exchanged zeolite Y at ambient temperature, Catal. Today 116 (2006) 526–529, https://doi.org/10.1016/j.cattod.2006.06.026.

[30] J.W. Hou, A.F. Sapnik, T.D. Bennett, Metal-organic framework gels and monoliths, Chem. Sci. 11 (2020) 310–323, https://doi.org/10.1039/c9sc04961d.

[31] B. Bueken, N.V. Velthoven, T. Willhammar, T. Stassin, I. Stassen, D.A. Keen, G. V. Baron, J.F.M. Denayer, R. Ameloot, S. Bals, D.D. Vos, T.D. Bennett, Gel-based morphological design of zirconium metal-organic frameworks, Chem. Sci. 8 (2017) 3939 3948, https://doi.org/10.1039/c6sc05602d.

[32] Standard Test Method for Determination of Trace Hydrogen Sulfide, Carbonyl Sulfide, Methyl Mercaptan, Carbon Disulfide and Total Sulfur in Hydrogen Fuel by Gas Chromatography and Sulfur Chemiluminescence Detection : ASTM D7652-11.

[33] Accelrys, Materials Studio, Modeling Getting Started, Accelrys Software Inc., San Diego, CA, 2004.

[34] J. Sanz, J.M. Serratosa, Silicon-29 and aluminum-27 high-resolution MAS-NMR spectra of phyllosilicates, J. Am. Chem. Soc. 106 (1984) 4790–4793, https://doi.org/10.1021/ja00329a024.

[35] H.J. Park, M.P. Suh, Enhanced isosteric heat, selectivity, and uptake capacity of $CO_2$ adsorption in a metal-organic framework by impregnated metal ions, Chem. Sci. 2 (2013) 685–690, https://doi.org/10.1039/C2SC21253F.

[36] L.C. Lin, D. Paik, J. Kim, Understanding gas adsorption in MOF-5/graphene oxide composite materials, Phys. Chem. Chem. Phys. 19 (2017) 11639–11644, https://doi.org/10.1039/C7CP00066A.

[37] C. Petit, T.J. Bandosz, MOF-graphite oxide composites: combining the uniqueness of graphene layers and metal-organic frameworks, Adv. Mater. 21 (2009) 4753–4757, https://doi.org/10.1002/adma.200901581.

[38] A.E. Amooghin, M. Omidkhah, H. Sanaeepur, A. Kargari, Preparation and characterization of $Ag^+$ ion-exchanged zeolite-Matrimid®5218 mixed matrix membrane for $CO_2/CH_4$ separation, J. Eng. Chem. 25 (2016) 450–462, https://doi.org/10.1016/j.jechem.2016.02.004.

[39] D.Z. Yi, H. Huang, X. Meng, L. Shi, Adsorption-desorption behavior and mechanism of dimethyl disulfide in liquid hydrocarbon streams on modified Y zeolites, Appl. Catal., B 148–149 (2014) 377–386, https://doi.org/10.1016/j.apcatb.2013.11.027.

[40] Y.F. Sun, M. Ma, B. Tang, S. Li, L. Jiang, X.H. Sun, M.L. Que, C.B. Tao, Z.T. Wu, Graphene modified Cu-BTC with high stability in water and controllable selective adsorption of various gases, J. Alloys Compd. 808 (2019) 151721–151730, https://doi.org/10.1016/j.jallcom.2019.151721.

[41] Q.M. Fu, J. Ding, W.L. Wang, J.F. Lu, Q.H. Huang, Carbon dioxide adsorption over amine-functionalized MOFs, Energy Proc. 142 (2017) 2152–2157, https://doi.org/10.1016/j.egypro.2017.12.620.

[42] B.C. Sun, S. Kayal, A. Chakraborty, Study of HKUST (Copper benzene-1,3,5-tricarboxylate, Cu-BTC MOF)-1 metal organic frameworks for $CH_4$ adsorption: an experimental Investigation with GCMC (grand canonical Monte-carlo) simulation, Energy 76 (2014) 419–427, https://doi.org/10.1016/j.energy.2014.08.033.

[43] T. Imyen, E. Znoutine, D. Suttipat, P. Iadrat, P. Kidkhunthod, S. Bureekaew, C. Wattanakit, Methane utilization to methanol by a hybrid Zeolite@Metal-organic framework, ACS Appl. Mater. Interfaces 12 (2020) 23812–23821, https://doi.org/10.1021/acsami.0c02273.

[44] G.H. Zhu, R. Graver, L. Emdadi, B.Y. Liu, K.Y. Choi, D.X. Liu, Synthesis of zeolite@metal-organic framework core-shell particles as bifunctional catalysts, RSC Adv. 4 (2014) 30673–30676, https://doi.org/10.1039/C4RA03129F.

[45] Q.A. Naddaf, H. Thakkar, F. Rezaei, Novel zeolite-5A@MOF-74 composite adsorbents with core-shell structure for $H_2$ purification, ACS Appl. Mater. Interfaces 10 (2018) 29656–29666, https://doi.org/10.1021/acsami.8b10494.
[46] F. Zhao, W.X. Yang, Y. Han, X.L. Luo, W.Z. Tang, T.L. Yue, Z.H. Li, A straightforward strategy to synthesize supramolecular amorphous zirconium metal-organic gel for efficient Pb(II) removal, Chem. Eng. J. 407 (2021), 126744, https://doi.org/10.1016/j.cej.2020.126744.
[47] S.C. Gu, T.H. Kondo, E. Mine, D. Nagao, Y. Kobayashi, M. Konno, Fabrication of sub-micrometer-sized jingle bell-shaped hollow spheres from multilayered core-shell particles, J. Colloid Interface Sci. 279 (2004) 281–283, https://doi.org/10.1016/j.jcis.2004.06.037.
[48] M. Fallah, S. Sohrabnezhad, Study of synthesis of mordenite zeolite/MIL-101 (Cr) metal-organic framework compounds with various methods as bi-functional adsorbent, Adv. Powder Technol. 30 (2019) 336–346, https://doi.org/10.1016/j.apt.2018.11.011.
[49] H. Song, X.H. Cui, H.L. Song, H.J. Gao, F. Li, Characteristic and adsorption desulfurization performance of Ag-Ce bimetal ion-exchanged Y zeolite, Ind. Eng. Chem. Res. 53 (2015) 14552–14557, https://doi.org/10.1021/ie404362f.
[50] J. Scherzer, J.L. Bass, Infrared spectra of ultrastable zeolites derived from type Y zeolites, J. Catal. 28 (1973) 101–115, https://doi.org/10.1016/0021-9517(73)90184-X.
[51] T.M. Salama, I. Othman, M. Sirag, G.A. Ei-Shobaky, Comparative study of molybdenum oxide in NaY zeolite prepared by conventional Impregnation and vapor-phase deposition techniques, Microporous Mesoporous Mater. 95 (2006) 312–320, https://doi.org/10.1016/j.micromeso.2006.06.004.
[52] K. Hadjiivanov, E. Lvanova, H. Knozinger, FTIR study of low temperature CO adsorption on Y zeolite exchanged with $Be^{2+}$, $Mg^{2+}$, $Ca^{2+}$, $Sr^{2+}$ and $Ba^{2+}$ cations, Microporous Mesoporous Mater. 58 (2003) 225–236, https://doi.org/10.1016/S1387-1811(02)00650-9.
[53] J. Zhang, Y.Y. Chu, X.L. Liu, H. Xu, X.J. Meng, Z.C. Feng, F.S. Xiao, Interzeolite transformation from FAU to CHA and MFI zeolites monitored by UV Raman spectroscopy, Chin. J. Catal. 40 (2019) 1854–1859, https://doi.org/10.1016/S1872-2067(19)63287-0.
[54] C. Petit, J. Burress, T.J. Bandosz, The synthesis and characterization of copper-based metal-organic framework/graphite oxide composites, Carbon 49 (2011) 563–572, https://doi.org/10.1016/j.carbon.2010.09.059.
[55] B. Erdem, R.A. Hunsicker, G.W. Simmons, E.D. Sudol, V.L. Dimonie, M.S. Ei-Aasser, XPS and FTIR surface characterization of $TiO_2$ particles used in polymer encapsulation, Langmuir 17 (2001) 2664–2669, https://doi.org/10.1021/la0015213.
[56] C. Prestipino, L. Refli, J.G. Vitillo, F. Bonino, A. Damin, C. Lamberti, A. Zecchina, P. L. Solari, K.O. Kongshaug, S. Bordiga, Local structure of framework Cu(II) in HKUST-1 metalorganic framework: spectroscopic characterization upon activation and interaction with adsorbates, Chem. Mater. 18 (2006) 1337–1346, https://doi.org/10.1021/cm052191g.
[57] N.R. Dhumal, M.P. Singh, J.A. Anderson, J. Kiefer, H.J. Kim, Molecular interactions of a Cu-Based metal-organic framework with a confined imidazolium-based ionic liquid: a combined density functional theory and experimental vibrational spectroscopy study, J. Phys. Chem. C 120 (2016) 3295–3304, https://doi.org/10.1021/acs.jpcc.5b10123.
[58] D. Wang, H. Jang, J.L. Tan, Y.X. Chen, Y. An, Y.H. Chen, Y. Wu, C.L. Liu, H. Sun, J. C. Liu, D. Wu, B.X. Shen, Manipulating oxidation states of copper within Cu-BTC using $Na_2S_2O_3$ as a new strategy for enhanced adsorption of sulfide, Ind. Eng. Chem. Res. 58 (2019) 19503–19510, https://doi.org/10.1021/acs.iecr.9b04349.
[59] A. Sahai, N. Goswami, S.D. Kaushik, S. Tripathi, Cu/$Cu_2O$/CuO nanoparticles: novel synthesis by exploding wire technique and extensive characterization, Appl. Surf. Sci. 390 (2016) 974–983, https://doi.org/10.1016/j.apsusc.2016.09.005.
[60] C. Li, C. Yang, S.C. Xu, C. Zhang, Z. Li, X.Y. Liu, S.Z. Jiang, Y.Y. Huo, A.H. Liu, B. Y. Man, $Ag_2O$@Ag core-shell structure on PMMAas low-cost and ultra-sensitive flexible surface-enhanced Raman scattering substrate, J. Alloys Compd. 695 (2017) 1677–1684, https://doi.org/10.1016/j.jallcom.2016.10.317.
[61] Y. Wang, Y.N. Miao, S. Li, L.J. Gao, G.M. Xiao, Metal-organic frameworks derived bimetallic Cu-Co catalyst for efficient and selective hydrogenation of biomass-derived furfural to furfuryl alcohol, Mol. Catal. 436 (2017) 128–137, https://doi.org/10.1016/j.mcat.2017.04.018.
[62] J.M. Yu, L.H. Xie, J.R. Li, Y.G. Ma, J.M. Seminario, P.B. Balbuena, $CO_2$ capture and separations using MOFs: computational and experimental studies, Chem. Rev. 117 (2017) 9674–9754, https://doi.org/10.1021/acs.chemrev.6b00626.
[63] J.K. Xie, N.Q. Yan, Z. Qu, S.J. Yang, Synthesis, characterization and experimental investigation of Cu-BTC as $CO_2$ adsorbent from flue gas, J. Environ. Sci. 24 (2012) 640–644, https://doi.org/10.1016/S1001-0742(11)60841-3.
[64] J. Bu, G. Loh, C.G. Gwie, S. Dewiyanti, M. Tasrif, A. Borgna, Desulfurization of diesel fuels by selective adsorption on activated carbons: competitive adsorption of polycyclic aromatic sulfur heterocycles and polycyclic aromatic hydrocarbons, Chem. Eng. J. 166 (2011) 207–217, https://doi.org/10.1016/j.cej.2010.10.063.
[65] X. Chen, B.X. Shen, H. Sun, G.X. Zhan, Z.Z. Huo, Adsorption and its mechanism of CS2 on ion-exchanged zeolites Y, Ind. Eng. Chem. Res. 56 (2017) 6499–6507, https://doi.org/10.1021/acs.iecr.7b00245.
[66] X. Chen, B.X. Shen, H. Sun, G.X. Zhan, Ion-exchanged zeolites Y for selective adsorption of methyl mercaptan from natural gas: experimental performance evaluation and computational mechanism explorations, Ind. Eng. Chem. Res. 56 (2017) 10164–10173, https://doi.org/10.1021/acs.iecr.7b01982.
[67] Y.W. Zhao, B.X. Shen, H. Sun, Adsorptive removal of dimethyl disulfide from methyl tert-butyl ether using an Ag-exchanged ZSM-5 zeolite, RSC Adv. 6 (2016) 93086–93093, https://doi.org/10.1039/C6RA17741G.
[68] J.H. Kim, X.L. Ma, A. Zhou, C.S. Song, Ultra-deep desulfurization and denitrogenation of diesel fuel by selective adsorption over three different adsorbents: a study on adsorptive selectivity and mechanism, Catal. Today 111 (2006) 74–83, https://doi.org/10.1016/j.cattod.2005.10.017.
[69] Y.W. Li, F.H. Yang, G.S. Qi, R.T. Yang, Effects of oxygenates and moisture on adsorptive desulfurization of liquid fuels with Cu(I)Y zeolite, Catal. Today 116 (2006) 512–518, https://doi.org/10.1016/j.cattod.2006.06.037.